1   **Convergence of unisensory-evoked signals via multiple pathways to the cerebellum**

2

3   Misa Shimuta[1], Izumi Sugihara[2], Taro Ishikawa[1]*

4

5   [1] Department of Pharmacology, The Jikei University School of Medicine, Tokyo, Japan

6   [2] Department of Systems Neurophysiology, Tokyo Medical and Dental University Graduate School

7   of Medical and Dental Sciences, Tokyo, Japan

8

9   *Address for correspondence:

10   taroishi@gmail.com

11   Department of Pharmacology, The Jikei University School of Medicine

12   3-25-8 Nishi-Shinbashi, Minato-ku, Tokyo, 105-8461, Japan

13   Tel: +81 (0)3 5400 1200(ex 2251)

14

15   **SUMMARY**

16   The cerebellum receives signals directly from peripheral sensory systems and indirectly from the

17   neocortex. To reveal how these different types of signals are processed in the cerebellar cortex, *in*

18   *vivo* whole-cell recordings from granule cells and unit recordings from Purkinje cells were

19   performed in mice in which primary somatosensory cortex (S1) could be optogenetically inhibited.

20   Tactile stimulation of the upper lip produced two-phase granule cell responses (with latencies of ~8

21   ms and 28 ms), for which only the late phase was S1 dependent. Complex spikes and the late

22   phase of simple spikes in Purkinje cells were also S1 dependent. These results indicate that

23   individual granule cells integrate convergent inputs from the periphery and neocortex, and send

24   their outputs to Purkinje cells, which then combine those signals with climbing fiber signals from

25   the neocortex.

26

27   **INTRODUCTION**

28   The cerebellum and neocortex are interconnected by a large fiber system (Schmahmann et al.,

29   2019; Watson and Apps, 2019). Although the basal ganglia similarly connect with the neocortex,

30   the cerebellum receives inputs not only from the neocortex but also from the peripheral sensory

31   systems, including tactile, proprioceptive, and vestibular systems (Bostan et al., 2013). How the

32   cerebellum integrates these signals is not well understood.

33   The cerebellum receives inputs via two types of projection fibers, namely, mossy fibers that

34   project to granule cells and climbing fibers that project to Purkinje cells. A major subgroup of the

35   mossy fibers projects from the pontine nuclei (basilar pontine nuclei and nucleus reticularis

36   tegmenti pontis), which relay signals from the neocortex (Kratochwil et al., 2017; Leergaard and

37   Bjaalie, 2007; Morissette and Bower, 1996). Other mossy fibers originate in the spinal cord and

38 brainstem nuclei, including the trigeminal nuclei, and relay sensory signals directly from the

39 periphery (Sillitoe et al., 2012). Beginning in the 1970s, it was shown that spinal and trigeminal

40 mossy fibers transmitting somatosensory signals from a body part and the corticopontine mossy

41 fibers transmitting signals from the corresponding somatotopic area in the somatosensory cortex

42 terminate in the same areas in the cerebellum (Allen and Tsukahara, 1974; Allen et al., 1974;

43 Bower et al., 1981; Morissette and Bower, 1996; Provini et al., 1968; Tahon et al., 2011). However,

44 at the single-cell level, it is still not clear whether these inputs project to different groups of granule

45 cells (Allen et al., 1974; Tahon et al., 2011) or converge on the same individual granule cells. This

46 issue is important in order to understand the basis of cerebellar computation.

47   Cerebellar granule cells are small electrically compact cells that receive synaptic inputs

48 from a small number (on average, four) of mossy fibers. Conversely, a single mossy fiber projects

49 to a much larger number (several hundred or more) of granule cells. Thus, Marr and Albus

50 independently proposed similar ideas that the mossy fiber-granule cell system expands the neural

51 representation of information (Albus, 1971; Marr, 1969). This idea, called the expansion recoding

52 hypothesis, assumes that each granule cell receives inputs from a near-random combination of

53 mossy fibers that convey different types of signals, thereby creating numerous combination

54 patterns. Although experimental approaches to test this hypothesis have been hampered by

55 difficulties in tracing individual mossy fibers and recording from single granule cells *in vivo*, more

56 recent studies utilizing neuronal labeling (Huang et al., 2013), *in vivo* electrophysiology (Ishikawa

57 et al., 2015), and *in vitro* electrophysiology combined with neuronal labeling (Chabrol et al., 2015)

58 have demonstrated that mossy fiber inputs conveying different sensory or motor signals converge

59 onto single granule cells. However, the fundamental issue of whether signals evoked by a

60 particular sensory stimulus can converge onto single granule cells after traveling via different

61 pathways has not been investigated.

62   The cerebellar cortex also receives inputs from climbing fibers, which originate solely from

63 the inferior olivary nuclei. These nuclei comprise a large complex of subnuclei whose inputs have

64 not fully been revealed, but they are known to receive indirect inputs from the neocortex and thus

65 may provide another pathway for cerebrocerebellar communication (Allen et al., 1974; Brown and

66 Bower, 2002; Provini et al., 1968; Ros et al., 2009; Sasaki et al., 1977). However, it has not been

67 demonstrated that the neocortex mediates sensory-evoked climbing fiber responses.

68   In the present study involving *in vivo* patch clamping and optogenetic manipulation, we

69 provide unequivocal functional evidence that direct trigeminal signals and indirect signals from the

70 primary somatosensory cortex (S1) converge onto the same granule cells. We also show that this

71 integration affects spike outputs of not only the granule cells but also the Purkinje cells.

72 Furthermore, we show that the climbing fiber inputs to Purkinje cells also depend on activity in S1.

73

74 **RESULTS**

75   **Photoinhibition of S1 suppresses the late component of cerebellar sensory responses**

76   To investigate how inputs from S1 influence activity in the cerebellar cortex, we recorded field

77   potentials simultaneously from S1 and the granule cell layer (GCL) of the cerebellar cortex in

78   transgenic mice expressing channelrhodopsin 2 (ChR2) in GABAergic neurons (VGAT-ChR2 mice)

79   (Figures 1A and 1B). In mice anesthetized with ketamine/xylazine, a brief (50 ms) air puff applied

80   to the upper lip evoked large responses both in the upper lip area of S1 (3.8–4.5 mm lateral and 0–

81   1.0 mm rostral to bregma) and in the GCL of the crus II area. Similarly to that reported in rats

82   (Morissette and Bower, 1996), the responses in the GCL had two peaks, namely, early and late

83   peaks (8.3 ± 0.3 ms and 28.8 ± 0.7 ms [mean ± SEM] from the onset of stimulation, respectively, n

84   = 15) that appeared before and after the peak of S1 (25.2 ± 1.2 ms, n = 15), respectively (Figures

85   1C and 1D). When S1 activity was suppressed by focal illumination with blue light in alternating

86   trials, the response of S1 and the late (but not early) component of the GCL response were

87   eliminated (Figures 1C and 1D), indicating that the late component of the GCL response depends

88   on the activity of S1. For this and subsequent experiments, a continuous 150 ms light stimulus was

89   applied during sensory stimulation, but a longer or shorter light stimulus was similarly effective

90   (Figure S1). In similar experiments performed in awake (head-fixed) mice, the early component of

91   the GCL response had two peaks (at 5.1 ± 0.2 ms and 13.0 ± 0.3 ms from the onset of stimulation,

92   n = 9), and the S1 response peaked at 14.2 ± 1.0 ms (n = 9). The late component of the GCL

93   response, which was measured during a fixed time window (18–23 ms after the onset of

94   stimulation), was eliminated by S1 photoinhibition (Figures 1E and 1F). Of note, the late

95   component was much smaller in awake mice than in anesthetized mice, presumably due to

96   desynchronization in S1 under the awake condition (see Discussion). In a separate set of

97   experiments, anesthetics other than ketamine/xylazine had suppressive effects on both the S1

98   response and the late component of the GCL response (Figure S2). Therefore, we used

99   ketamine/xylazine in subsequent experiments. Ketamine/xylazine has only minor effects on mossy

100   fiber-granule cell synapses and tonic inhibition of granule cells (Bengtsson and Jörntell, 2007;

101   Duguid et al., 2012).

102   To identify the neocortical region involved in the cerebellar response, we performed the

103   same experimental protocol but with the optrode at various loci of the neocortex. The late

104   component of the GCL response was suppressed most effectively by photoinhibition of the locus

105   where the S1 response was largest (3.8 mm lateral and 0 mm rostrocaudal from bregma) but not

106   suppressed by photoinhibition at distant loci, including the primary motor cortex (M1) (Figure 1G).

107   This result suggested that S1 projects directly to the pons, without a relay through other neocortical
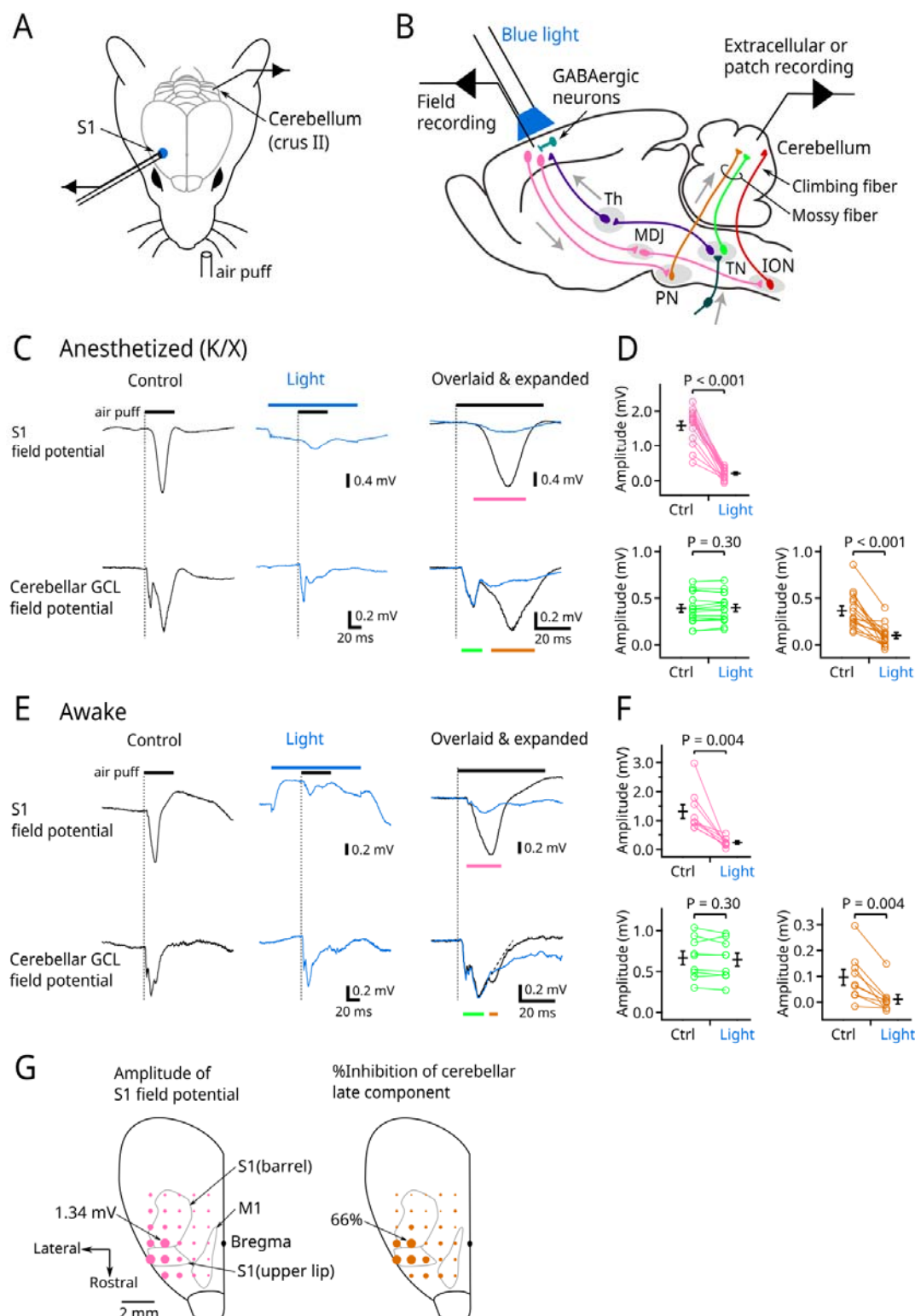
108   areas.

Figure 1. Optogenetic inhibition of S1 suppresses the late component of the cerebellar sensory response.

(A) Experimental configuration. Tactile stimulation (air puff) was applied to the left upper lip while field potentials were recorded from the GCL of the ipsilateral crus II area of the cerebellum and the upper lip area of the contralateral S1. S1 was optogenetically suppressed in alternating trials.

4

114   (B) Schematic of the neural circuit involved in this study. Th, thalamus; MDJ, mesodiencephalic
115   junction; PN, pontine nuclei; TN, trigeminal nuclei; ION, inferior olivary nucleus.
116   (C) Representative recordings from a mouse anesthetized with ketamine/xylazine; 20 traces for
117   each condition were averaged. The same traces are baseline adjusted and overlaid in an
118   expanded time scale in the panels on the right. Black and blue bars indicate the durations of air
119   puff and LED illumination, respectively. The vertical dotted lines indicate the onset of air puff.
120   (D) Pooled data from 15 anesthetized mice. Peak amplitudes were measured during the times
121   indicated by colored bars in (C).
122   (E) Similar to (C) except using an awake mouse; 46 traces for each condition were averaged. The
123   decay time course of the fast component of the cerebellar response was fitted and extrapolated by
124   a single exponential curve (the dashed line) in the panel on the right.
125   (F) Similar to (D) except using nine awake mice. The cerebellar late component was measured
126   after subtracting the decay component of the early response (see Methods).
127   (G) Left, bubble size indicates field potential amplitude at each spot measured in the right cerebral
128   hemisphere. Right, bubble size indicates magnitude of inhibition of the cerebellar late component
129   when blue light was applied to each spot. The cerebellar early component was not affected by
130   photoinhibition at any of these spots. Data from 15 animals were combined. Each spot is the
131   average from 3–15 animals. S1 for upper lip and barrel and the primary motor cortex (M1) are
132   illustrated in accordance with Allen Mouse Brain Atlas and (Mohajerani et al., 2013).
133   Means ± SEMs are presented as black bars and lines, respectively. See also Figures S1 and S2.
134

135   **_In vivo_ whole-cell recording from granule cells revealed convergent synaptic inputs**
136   The above-described results were consistent with the established theory that at least two distinct
137   groups of mossy fibers project to the GCL of crus II: one directly from the trigeminal nuclei and the
138   other via the cerebropontine pathway (Morissette and Bower, 1996; Steindler, 1985; Woolston et
139   al., 1981). To determine whether these two inputs converge onto individual granule cells, we
140   performed whole-cell patch-clamp recordings in anesthetized mice. In 50% (12/24) of granule cells,
141   excitatory postsynaptic currents (EPSCs) evoked by stimulation of the upper lip had two
142   components (as in the representative cell in Figure 2A), indicating that two types of mossy fibers
143   converge on some individual cells. However, other granule cells had conspicuous EPSCs with only
144   early (12.5%) or late (25%) timing, and the remainder (12.5%) had no response (cutoff, 0.5
145   events/trial) (Figure 2B). The numbers of EPSC events for the two components did not correlate (r
146   = 0.028, n = 24), suggesting that these connections were established independently. In these
147   recordings, it was noted that each component often had multiple EPSC events with very short
148   intervals (around 3 ms on average; Figure 2C). This is in line with previous studies showing that a
149   single mossy fiber can fire high-frequency bursts of action potentials that trigger high-frequency
150   EPSCs in granule cells (Chadderton et al., 2004; Rancz et al., 2007). Indeed, in our occasional
151   whole-cell recordings from putative mossy fiber boutons (n = 3), action potentials occurred in high-
152   frequency bursts with either early or late timing (Figure S3). Thus, the multiple EPSCs in each
153   component were likely derived from a single mossy fiber. Furthermore, as the interevent intervals
154   for the early and the late EPSC components did not differ (Figure 2C), it is likely that trigeminal and
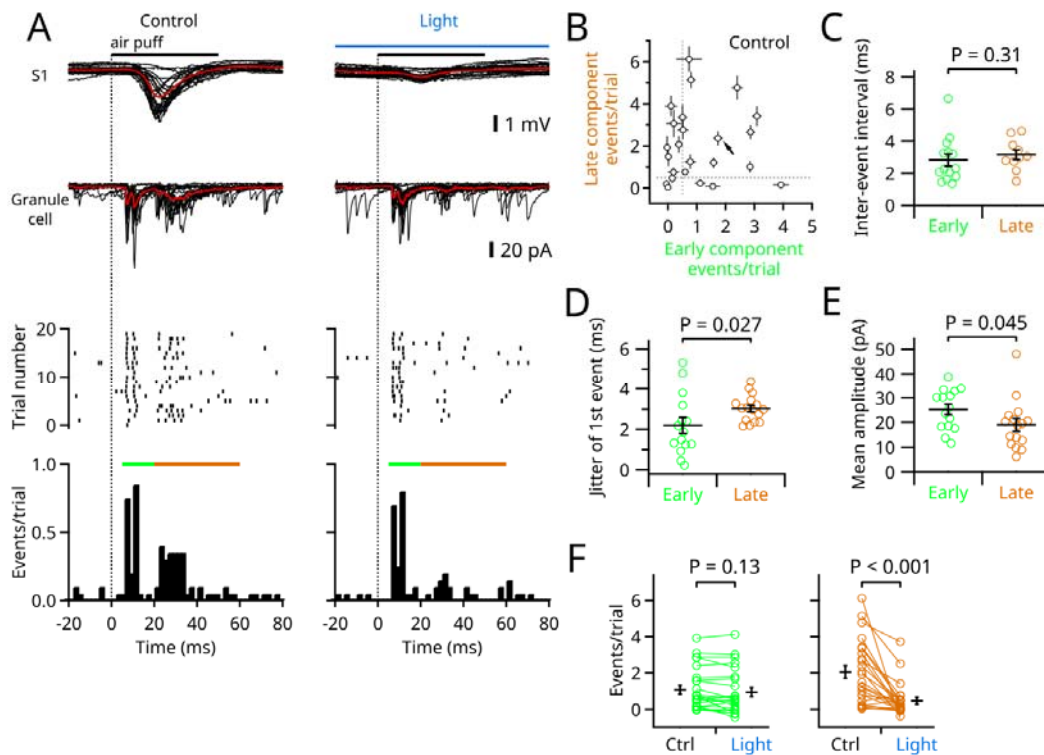
5

Figure 2. *In vivo* whole-cell recording from granule cells revealed convergent synaptic inputs.

(A) Representative recording; simultaneous field potential recording from S1 (top) and whole-cell voltage clamp recording from granule cell (lower); 20 consecutive traces are overlaid. The average traces are in red. Detected EPSC events are shown in raster plots (middle) and time histograms (bottom). Green and brown bars indicate the early and the late phases. Trials under control (left) and the light (right) conditions were interleaved.

(B) The numbers of evoked EPSC events in the early and the late phases were compared in 24 cells. The numbers were corrected for baseline spontaneous events by subtraction in this and the following panels. For qualitative description, event numbers of <0.5 events/trial (dotted lines) were defined as no response. Error bars indicate SEMs (trial-by-trial fluctuation). The arrow points to the cell shown in (A).

(C) The median interevent interval of each cell was compared (n = 14 in the early and n = 10 in the late).

(D) Trial-by-trail fluctuations (measured as standard deviation) of the timing of the first event during each time period were compared (n = 15 in the early and n = 16 in the late).

(E) The mean amplitudes of EPSCs in the early and late phases were compared (n = 15 in the early and n = 16 in the late).

(F) EPSC event numbers were compared for the early phase (left) and the late phase (right) (n = 24).

Means ± SEMs are presented as black bars and lines, respectively. See also Figures S3, S4, and S5.

pontine mossy fibers can fire similar high-frequency bursts. However, the fluctuation of the timings (jitter) of the first event was larger in the late component than in the early component (Figure 2D),

180   reflecting a longer multistep pathway for transmission of the late response. However, the amplitude

181   of individual EPSC events was larger for the early components (Figure 2E), suggesting that the

182   synaptic properties (i.e., quantal content and/or quantal size) may differ between these two types

183   of synaptic inputs, as reported previously for the various vestibular inputs (Chabrol et al., 2015). As

184   expected, the late component of EPSCs was mostly eliminated by optogenetic suppression of S1

185   (Figure 2F), confirming that the late component signal is derived from S1. Similar results were

186   obtained when synaptic charge (the area over the curve), instead of event number, was measured

187   as an indicator of synaptic strength (Figures S4A and S4B). Furthermore, spontaneous EPSCs

188   were partially blocked by the suppression of S1 (Figure S5). These results indicate that granule

189   cells receive convergent inputs from two types of mossy fibers, although the balance of these

190   inputs varies between cells. Additionally, we recorded inhibitory postsynaptic currents (IPSCs) in a

191   small number of granule cells (n = 4) to examine feed-forward inhibition from Golgi cells. IPSCs

192   also exhibited two components, and the late component was suppressed by light illumination of S1

193   (Figures S4C and S4D).

194

195   **Spike output of single granule cells *in vivo***

196   To investigate how synaptic inputs trigger action potentials in granule cells, we recorded

197   membrane potentials in current clamp (Figure 3A). The resting potentials of granule cells varied

198   widely (from -96.0 to -50.8 mV; mean, -72.9 ± 3.4 mV, n = 16). In cells that had a relatively

199   hyperpolarized resting potential, the excitatory postsynaptic potential (EPSP) did not reach the

200   spike threshold (Figure 3B), indicating that a single tactile stimulus generates a spike in only a

201   subset of the granule cells. As the resting potentials of granule cells are modulated by multiple

202   factors, such as tonic inhibition from Golgi cells and potassium channel function (Duguid et al.,

203   2012; Hamann et al., 2002; Millar et al., 2000), we applied steady depolarizing current (up to 20

204   pA) to 9 of the 16 cells, thereby raising the average resting potential to -57.2 ± 1.9 mV (n = 16,

205   including seven cells without adjustment) and increasing their propensity to fire in response to

206   tactile stimulation of the upper lip (11/16 cells fired action potentials; cutoff, 0.5 spikes/trial)

207   (Figures 3A and 3B). In this condition, the granule cells fired during the early or late phase (Figure

208   3C). As expected, action potentials in the late phase were eliminated by photoinhibition of S1

209   (Figure 3F). Investigation of the relationship between synaptic inputs and firing outputs showed

210   that the number of action potentials evoked in the early phase correlated with the number of EPSC

211   events during the same period (r = 0.77, n = 13) (Figure 3D, left). However, the correlation was

212   less clear in the late phase (r = 0.53, n = 13) (Figure 3D, right), suggesting that factors other than

213   instantaneous synaptic inputs may be involved. Indeed, depolarization during the early phase was

214   maintained through the late phase (Figure 3E). This suggests that action potential firing in the late
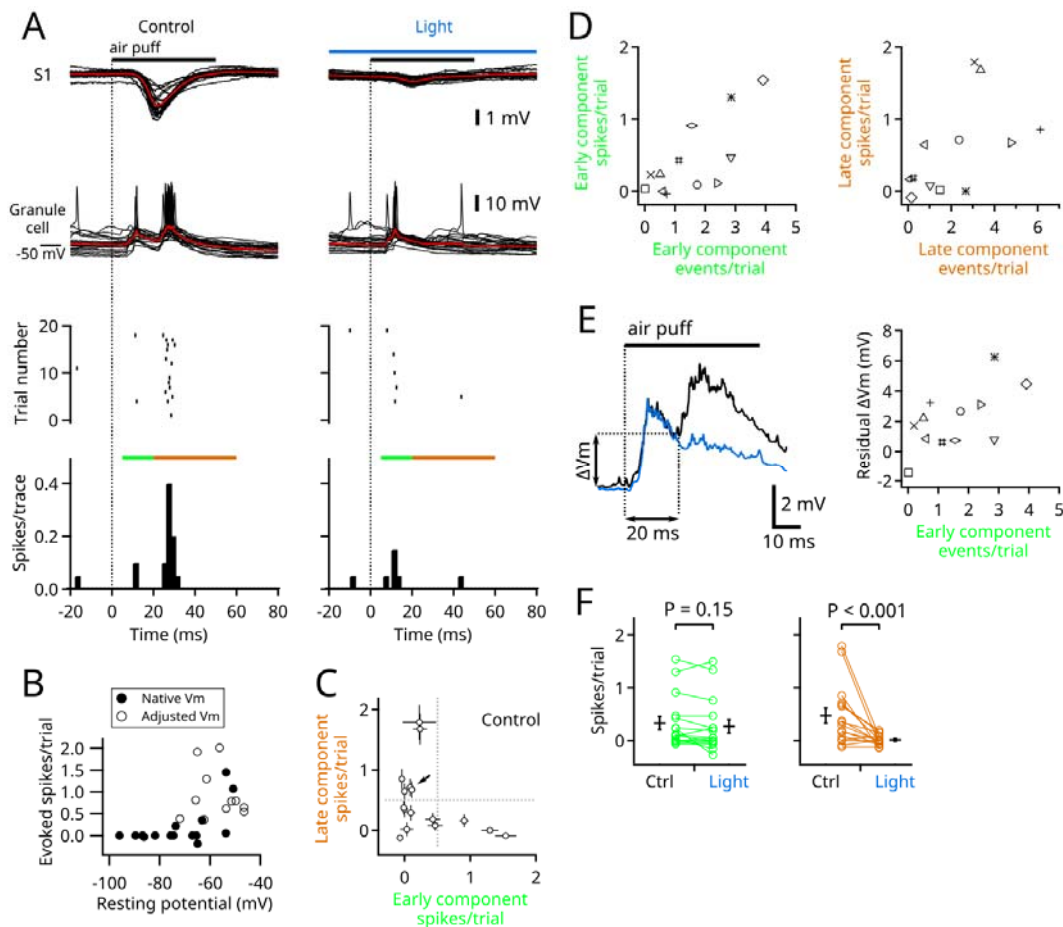
Figure 3. Spike output of single granule cells *in vivo*.

(A) Representative recordings of the same cell as in Figure 2A; simultaneous field potential recordings from S1 (top) and whole-cell current clamp recordings from a granule cell (lower); 20 traces are overlaid. The average traces are in red. Detected spikes are shown in raster plots (middle) and time histograms (bottom). Green and brown bars indicate the early and late phases. The trials under control (left) and light (right) conditions were interleaved.

(B) Numbers of evoked spikes (sums of the early and the late responses) plotted against the native resting potentials (filled circles, *n* = 16). In a subset of cells that had hyperpolarized native resting potentials (<65 mV), a steady depolarizing current was applied to facilitate firing (open circles, *n* = 9). The spike numbers were corrected for baseline spontaneous firing by subtraction in this and the following panels.

(C) The numbers of evoked spikes in the early and the late phases were compared in 16 cells, including three cells that lacked voltage clamp recording. For qualitative description, event numbers of <0.5 spikes/trial (dotted lines) were defined as no spikes. Error bars indicate SEMs (trial-by-trial fluctuation). The arrow points to the cell shown in (A).

(D) Numbers of evoked spikes in the early phase (left) and late phase (right) were plotted against the numbers of EPSCs during the same time periods. Individual cells (*n* = 13) are plotted as different marks common in (D) and (E).

(E) Left, averaged traces of all 16 granule cells in current clamp mode. Black, control; blue, photoinhibition of S1. Depolarization at 20 ms after the onset of stimulation was measured as residual depolarization. Right, the residual depolarization of each cell is plotted against the number

8

236   of EPSCs in the early phase.

237   (F) Evoked spike numbers were compared for the early phase (left) and the late phase (right) (*n* =

238   16). Means ± SEMs are presented as black bars and lines, respectively. See also Figure S6.

239

240   phase may be facilitated by temporal summation. A simulation in a realistic computational model of

241   a granule cell (Diwakar et al., 2009) showed such a facilitation (Figure S6).

242

243   **Sensory-evoked responses in granule cells in various parasagittal bands**

244   The cerebellar recording electrodes in the above-described experiments were positioned coarsely

245   around the 6+ band in crus II. To characterize the distribution of trigeminal and corticopontine

246   projections in crus II, we used Aldoc-Venus mice in which the various bands can be visualized

247   (Figure 4B). Field potentials were recorded from S1 simultaneously with *in vivo* whole-cell voltage

248   clamp recordings from the cerebellar granule cells in 5+, 5-, 6+, and 7+ bands. As observed in

249   VGAT-ChR2 mice, some granule cells had EPSCs in both early and late time periods, whereas

250   others had EPSCs in only one of these time periods (Figure 4A). Although early and late

251   responses were detected in all bands, the 7+ band had the fewest early component EPSC events,

252   and the fewest late component events were recorded in the 5- band (Figures 4C and S7B).

253   Consistent results were obtained with field potential recordings (Figure S7A). These results

254   indicate that the putative trigeminal and corticopontine mossy fiber inputs are variably distributed

255   over multiple bands in crus II. Furthermore, trial-by-trial analysis revealed a correlation between the

256   amplitude of the S1 response and the number of EPSC events in the late component but not in the

257   early component (Figures 4D and 4E), confirming that only the late component is S1 dependent.

258   Similar to that observed in VGAT-ChR2 mice, the mean EPSC amplitude was larger and the jitter

259   of the first event was smaller in the early response than in the late response, and the interevent

260   intervals did not differ (Figures S7C–E).

261

262   **Effect of S1 photoinhibition on SS and CS in Purkinje cells**

263   We next investigated how the suppression of S1 affects the firing of Purkinje cells, which are

264   downstream of granule cells in the cerebellar circuit (Bower and Woolston, 1983). In general,

265   simple spikes (SS) in Purkinje cells are generated spontaneously but are affected by excitatory

266   synaptic inputs from parallel fibers (i.e., granule cell axons) and inhibitory synaptic inputs from

267   molecular layer interneurons, whereas complex spikes (CS) are triggered solely by climbing fiber

268   inputs. Under control conditions (without S1 inhibition), there were four phases of SS in response

269   to stimulation of the upper lips of VGAT-ChR2 mice, namely, early excitatory (within 10 ms after

270   stimulation onset), early inhibitory (around 10–20 ms), late excitatory (around 20–30 ms), and late

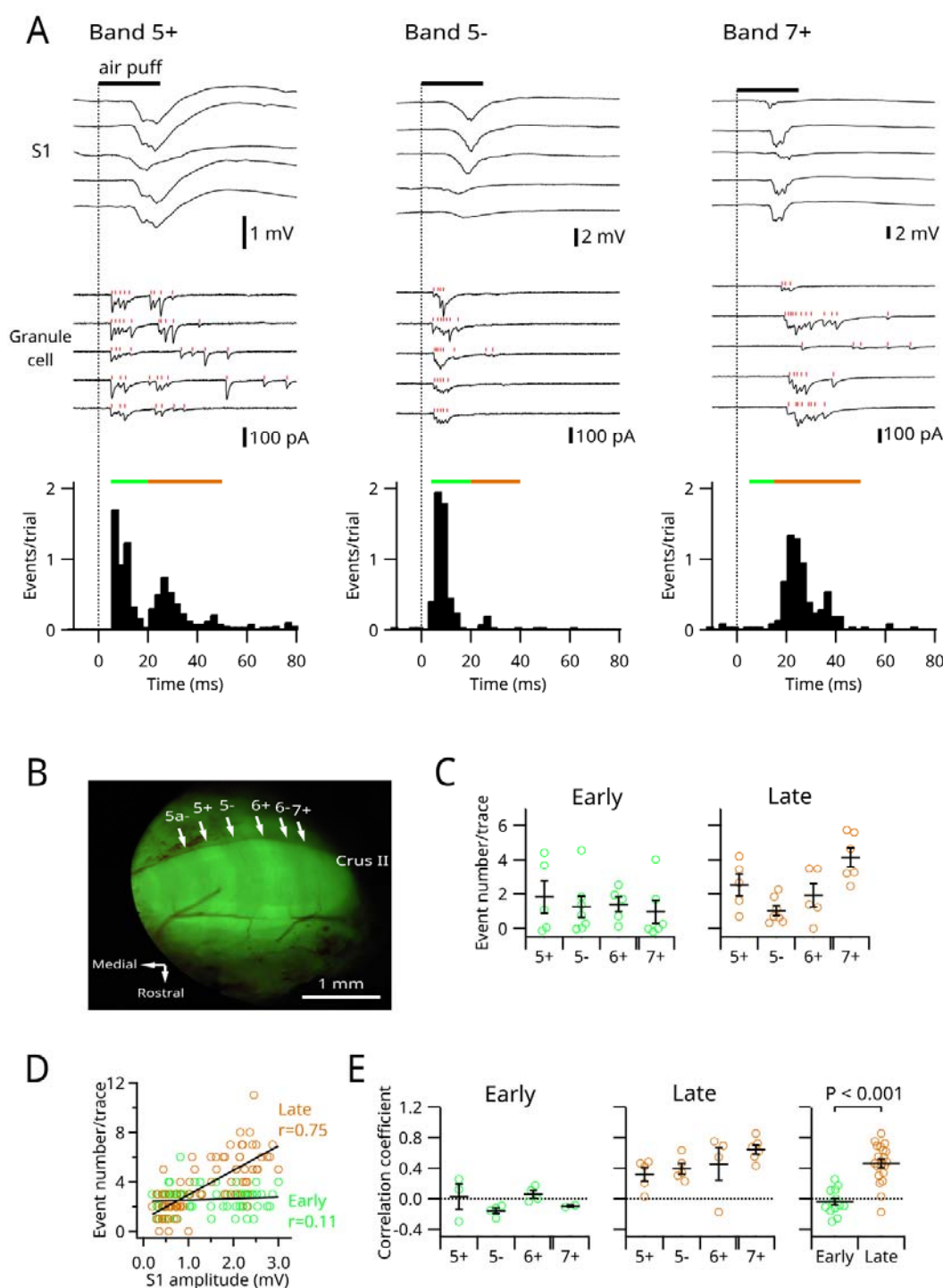271   inhibitory (30-60 ms) phases (Figures 5A–5D). CS coincided with the late inhibitory phase of SS.

272 **Figure 4. Sensory-evoked responses in granule cells in various parasagittal bands.**
273 (A) Representative recordings; simultaneous field potential recordings from S1 (top) and whole-cell
274 voltage clamp recordings from a granule cell (lower); five traces are displayed. Overlaid raster plots
275 in red indicate the timing of detected EPSC events. Time histograms are shown in the bottom
276 panels. Green and brown bars indicate the early and the late phases.
277 (B) Fluorescent macroscopic image of the cerebellar crus II area after removal of the dura mater.
278 (C) The numbers of EPSC events in different bands in the early (left) and the late (right) phases.

10

279 (D) Data from a sample cell in the 6+ band. The EPSC event numbers in the early (green) and late
280 (brown) phases in every trial were plotted against the amplitudes of S1 field responses. Correlation
281 coefficients were calculated for each phase.
282 (E) Correlation coefficients of all cells are plotted. The right panel shows pooled data from all
283 bands.
284 Means ± SEMs are presented as black bars and lines, respectively. See also Figure S7.

285

286 Photoinhibition of S1 did not affect the early phases of SS but eliminated the late excitatory and

287 inhibitory phases (Figures 5A–5D). Interestingly, the CS response was also abolished. These

288 results suggest that the direct trigeminal inputs to granule cells trigger the early excitatory and

289 inhibitory phases of SS, the latter of which presumably results from the activation of molecular

290 layer interneurons (Blot et al., 2016; Jelitai et al., 2016). These results also suggest that the late

291 excitatory responses of SS reflect inputs from S1. However, the late inhibitory response could

292 reflect either an interneuronal effect or a pause after CS. As CS did not always occur under the

293 control condition, we were able to separate traces with CS from those without (Figure S8). The late

294 inhibition phase of SS was larger in traces with CS than in those without CS, suggesting that the

295 late inhibition largely reflects the pause after CS. We also tested the effects of photoinhibition at

296 multiple loci in the neocortex and found that suppression of the upper lip area of the contralateral

297 S1 was most effective in blocking CS in Purkinje cells (Figure 5E). Furthermore, suppression of S1

298 with a long (10 s) light stimulus inhibited spontaneous CS firing and triggered rebound activation

299 after the light was turned off, suggesting that the spontaneous activity of the inferior olive is under

300 strong control of S1. However, this photoinhibition had no effect on SS firing (Figure S9),

301 suggesting that S1 activity is not directly linked to the spontaneous activity of granule cells (Figure

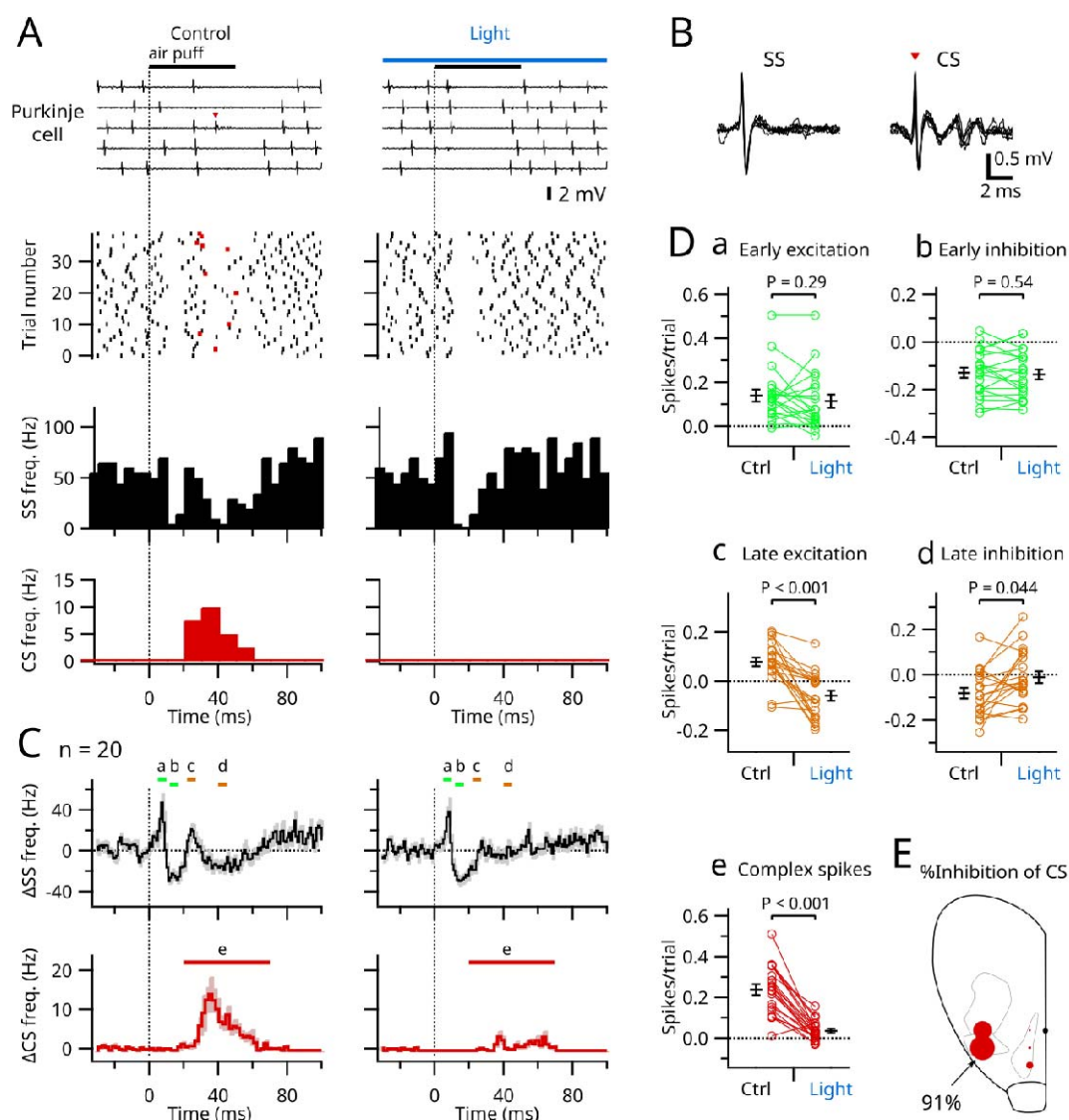302 S5) in line with a previous report (Ros et al., 2009).

11

Figure 5. Effects of S1 photoinhibition on SS and CS in Purkinje cells.

(A) Representative extracellular unit recordings of a Purkinje cell; five traces are displayed (top).
Simultaneous field potential recordings from S1 are not shown. SS (black) and CS (red) are plotted
in the raster plots (lower). Separate time histograms of SS (middle) and CS (bottom) are shown.
(B) Enlarged views of SS and CS of the unit shown in (A); six traces in each were aligned and
overlaid.
(C) Averaged time histograms of SS (1 ms bin) and CS (2 ms bin) from 20 Purkinje cells. Shading
indicates SEMs. Vertical dotted lines indicate the onset of stimulation as in (A).
(D) Spike numbers were measured during the times (a–e) indicated by colored bars in (C). Means
± SEMs are presented as black bars and lines, respectively.
(E) Bubble size indicates magnitude of inhibition of the cerebellar CS when the blue light was
applied to each spot in the right cerebral hemisphere. Only five spots were tested. Data from six
animals were combined. Each spot is the average from 3–6 animals.
See also Figures S8 and S9.

318 **DISCUSSION**

319 By taking advantage of the high temporal resolution of electrophysiology and optogenetics, we

320 obtained functional evidence that cerebellar granule cells in crus II receive inputs directly from the

321 periphery and indirectly via S1. We found that approximately half of the granule cells receive

322 convergent signals from both pathways. We also showed that the olivocerebellar inputs to these

323 Purkinje cells come through the same area in S1.

324

325 **Optogenetic analysis of the neural pathways**

326 We adopted an optogenetic method in which photostimulation of GABAergic neurons expressing

327 ChR2 can suppress the activity of specific areas of the neocortex (Guo et al., 2014; Li et al., 2015,

328 2016). This method is based on the fact that most GABAergic neurons in the neocortex are local

329 interneurons. Although 0.5% of GABAergic neurons project to other cortical and subcortical areas

330 (Tamamaki and Tomioka, 2010), it is unlikely that such long-range GABA projections contributed to

331 our findings because light illumination was effective only in specific areas in the neocortex (Figures

332 1G and 5E). Moreover, plenty of anatomical and physiological evidence indicates that the basal

333 pons relays signals from S1 to the cerebellar cortex (Leergaard and Bjaalie, 2007; Leergaard et al.,

334 2006; Morissette and Bower, 1996; Watson and Apps, 2019; Welker, 1987). Therefore, it is highly

335 likely that the late component of the cerebellar response in our study was transmitted via the

336 cortico-ponto-cerebellar pathway.

337

338 **Convergence of mossy fiber inputs to granule cells**

339 In contrast to the conventional view of Marr and Albus (Albus, 1971; Marr, 1969) that granule cells

340 receive inputs from mossy fibers carrying different types of information, it was recently proposed

341 that individual granule cells receive only one type of input (Bengtsson and Jörntell, 2009; Dean et

342 al., 2010; Spanne and Jörntell, 2015). Although both trigeminal and corticopontine signals were

343 evoked by the same tactile stimulation in our study, these signals are fundamentally different

344 because they can be differentially modulated on route to the cerebellum. For instance, neocortical

345 states (such as anesthesia and wakefulness) affected them differently (Figure 1), and they

346 exhibited different trial-to-trial fluctuations (Figure 4). Furthermore, as the S1 in mice sends efferent

347 motor signals directly to the brain stem (Matyas et al., 2010), the corticopontine signals we

348 observed may in fact be efferent copies of a motor command. Thus, since the distinctions between

349 trigeminal and corticopontine signals are substantial, our results are in line with the conventional

350 idea proposed by Marr and Albus.

351 As granule cells received either or both types of inputs, it is difficult to draw a unified view

352 for these connections. For the subpopulation of granule cells that receive both, our results (Figure

353 3E) indicate that depolarization during the early phase may facilitate firing in the late phase. In

354 such cases, the granule cells represent coincident detectors (i.e., an "AND" gate) and pattern

13

355   recoders as proposed by Marr and Albus. By contrast, granule cells that fire in response to a burst

356   of synaptic input from either a direct or S1-mediated connection may work as a simple relay or a

357   frequency filter (Bengtsson and Jörntell, 2009; Dean et al., 2010; Rancz et al., 2007). We

358   speculate that a granule cell can become an "OR" gate if both direct and S1-mediated inputs are

359   strong enough to trigger action potentials independently. An experimental system in which

360   trigeminal and corticopontine pathways can be activated independently is required to test this.

361   Previous morphological studies showed that aldolase-c-positive bands have more

362   corticopontine inputs than trigeminal or spinal ones, and that aldolase-c-negative bands have the

363   opposite trend (Biswas et al., 2019; Na et al., 2019), although there may be some overlap (Valera

364   et al., 2016). Our present results (Figures 4 and S7) are consistent with those studies, confirming

365   that different types of mossy fibers tend to innervate different compartments at the macroscopic

366   level. However, at the single-cell level, the strengths of these two types of inputs were neither

367   positively nor negatively correlated (Figure 2B), suggesting that two independent mossy fibers

368   synapse with a granule cell by chance, without attracting or repelling each other (Solowska et al.,

369   2002). The randomness of these connections is consistent with the expansion recoding hypothesis

370   of granule cells proposed by Marr and Albus (Cayco-Gajic and Silver, 2019).

371   An electrophysiological study using extracellular recording suggested that the GCL has a

372   stratified organization in which the trigeminal mossy fibers are located deeper than the

373   corticopontine mossy fibers (Tahon et al., 2011). Although our results do not directly contradict this

374   idea, they strongly suggest that the trigeminal and corticopontine mossy fibers largely overlap in

375   the GCL even if they tend to be distributed at different depths. Future studies, such as those using

376   functional cellular imaging (Giovannucci et al., 2017; Wagner et al., 2017, 2019), may elucidate the

377   detailed organization of the GCL.

378   As there are extensive studies regarding inhibitory inputs to granule cells from Golgi cells

379   (Duguid et al., 2012, 2015; Tabuchi et al., 2018; Vos et al., 1999), we performed only a few

380   experiments on IPSCs in this study. We found that, like EPSCs, the IPSC events had two phases.

381   These currents were delayed in relation to EPSCs by only a few milliseconds, reflecting rapid feed-

382   forward inhibition from Golgi cells. The importance of the excitation/inhibition balance in granule

383   cells has been discussed elsewhere (D'Angelo et al., 2013; Mapelli et al., 2014).

384

385   **Convergence of inputs to Purkinje cells**

386   We found that Purkinje cells receive signals from the neocortex not only via the mossy fiber-

387   parallel fiber pathway but also via climbing fibers. This finding is consistent with anatomical

388   observations that Purkinje cells in the 6+ compartment (D1 band) receive inputs from climbing

389   fibers from the ventral principal olive, which receives inputs from the area parafascicularis

390   prerubralis in the mesodiencephalic junction, which, in turn, receives projections from the

391   neocortex (Carlton et al., 1982; Naus et al., 1985; Sugihara and Shinoda, 2004). Our present study

14

392 is also in line with classical physiological studies showing a convergence of mossy and climbing

393 fiber signals originating from the same neocortical areas in cats and monkeys (Allen et al., 1974;

394 Provini et al., 1968; Sasaki et al., 1977) as well as a more recent study showing that injections of

395 lidocaine into the somatosensory cortex delayed the timing of CS in crus II in rats (Brown and

396 Bower, 2002). Still, our present study is the first to clearly demonstrate that S1 mediates sensory-

397 evoked climbing fiber responses. In contrast to what we observed, a recent study (Kubo et al.,

398 2018) reported that inhibition of the somatosensory cortex in mice did not inhibit CS. The reason

399 for this discrepancy is unclear but may involve minor differences in sensory stimulation,

400 optogenetic methods, or the sites recorded.

401   The physiological significance of this cortio-olivo-cerebellar connection is intriguing,

402 especially given the parallel cortico-ponto-cerebellar connection. This circuitry suggests that the

403 neocortex exerts powerful control over cerebellar signal processing. For instance, it may be

404 possible that signals from the neocortex induce synaptic plasticity at synapses on Purkinje cells

405 when parallel and climbing fibers are activated simultaneously via the respective cortico-ponto-

406 cerebellar and cortio-olivo-cerebellar pathways. Such top-down signaling may occur not only

407 during wakefulness but also during sleep as offline activity (Miyamoto et al., 2016; Ramanathan et

408 al., 2015).

409

410 **Limitations and future directions**

411 One limitation of the present study is that the data were largely obtained from animals anesthetized

412 with ketamine/xylazine, which has a suppressive effect on parallel fiber-Purkinje cell synapses

413 (Bengtsson and Jörntell, 2007; Duguid et al., 2012). However, the sensory stimulation applied was

414 able to evoke SS in Purkinje cells. Ketamine/xylazine also synchronizes activity in the neocortex

415 (Pachitariu et al., 2015), which may enhance the size and distribution of cortical responses to a

416 punctuate stimulus (Harris and Thiele, 2011; Poulet and Crochet, 2018). The fact that S1-mediated

417 signals observed in the cerebellum were clearer (larger and better isolated) in anesthetized

418 animals than in awake animals (Figure 1) may be attributable to this effect. As the precise

419 mechanisms of action of the anesthetics are not known, further studies are required to understand

420 how brain states, including natural sleep, affect cerebrocerebellar communication.

421   A second limitation is that we did not have a method to specifically block the trigemino-

422 cerebellar pathway. A future challenge is to manipulate the trigeminal neurons projecting to the

423 cerebellum without affecting those projecting to the thalamus. This may be possible in principle as

424 those neurons may be different populations in the trigeminal nuclei (Bennett-Clarke et al., 1992;

425 Zhang et al., 2018). On a related note, we do not know whether the early phase inputs from the

426 trigeminal nuclei to the cerebellar granule cells were monosynaptic or polysynaptic. Although these

427 responses had very short latencies, it is possible that rapid polysynaptic inputs, relayed within the

428 trigeminal nuclei or in other brainstem areas, contributed. Indeed, the early responses in awake

15

429   mice had two clear peaks. In this study, we collectively referred to these early responses as the

430   direct trigeminal response to distinguish them from the indirect S1-mediated response.

431   Finally, in this study, the only sensory stimulus was tactile stimulation (air puff) of the upper

432   lip. We adopted this form of stimulation because it gave large responses in both S1 and the

433   cerebellum. However, tactile stimulation of other body parts or stimulation of other modalities may

434   similarly evoke multipathway responses in the cerebellar cortex. Given the extensive connections

435   between the neocortex and the cerebellum (Leergaard and Bjaalie, 2007; Proville et al., 2014), it is

436   likely that similar circuits exist for the sensation of other types of stimulation.

437

438   **METHODS**

Key resources table		
Chemicals		
N/A		
Organisms/Strains		
Mouse: VGAT-ChR2-EYFP	The Jackson Laboratory	RRID: IMSR_JAX:014548
Mouse: Aldoc-Venus	Izumi Sugihara	MGI:3609644
Mouse: C57BL/6N	Japan SLC	N/A
Software and Algorithms		
Igor Pro	Wavemetrics	https://www.wavemetrics.com/
TaroTools	Taro Ishikawa	https://sites.google.com/site/tarotoolsregister/

439

440   **Animals**

441   All animal procedures were approved by the Institutional Animal Care and Use Committee of The

442   Jikei University (no. 2015-054 and 2017-001) under the Guidelines for the Proper Conduct of

443   Animal Experiments of the Science Council of Japan (2006).

444   Hemizygous transgenic mice (3–8 weeks old, male and female) expressing modified ChR2

445   (hChR2-H134R) fused with YFP in GABAergic neurons via the vesicular GABA transporter

446   promoter/enhancer (VGAT-ChR2 mice, stock no. 014548; Jackson Laboratory) (Zhao et al., 2011)

447   were used in photoinhibition experiments. Heterozygous knock-in mice (3–5 weeks old, male and

448   female) expressing Venus fluorescent protein via the aldolase-C promoter (Aldoc-Venus mice,

449   MGI:3609644) (Fujita et al., 2014) were used to visually identify the cerebellar parasagittal zones.

450

451   **Surgery**

16

452 The mice were anesthetized with an initial dose of a mixture of ketamine (86 mg/kg body weight)

453 and xylazine (10 mg/kg), and supplemented with a continuous infusion of ketamine (70 mg/kg/h)

454 and xylazine (8 mg/kg/h) via a syringe pump to maintain a stable level of anesthesia with free

455 breathing. The heads of mice were fixed in position via a head post glued onto the skull. Core body

456 temperature was maintained at around 37□C with an isothermic feedback heating pad. After

457 removing the overlaying skin and muscles, a craniotomy was performed over the left cerebellar

458 crus II area and the right cerebral somatosensory area. After removing the dura, the exposed brain

459 surface was kept moist with a HEPES-buffered saline containing (in mM) NaCl 150, KCl 2.5,

460 HEPES 10, $CaCl_2$ 2, and $MgCl_2$ 1 (pH adjusted to 7.4 with NaOH). To record from awake mice, the

461 head post was attached during a surgery 3 days before recording. Craniotomies were performed

462 under isoflurane anesthesia on the recording day. The mice were habituated to the recording

463 environment for >1 h before the start of recording. The duration of the recording session was <5 h

464 for each animal.

465

466 **Recording**

467 Whole-cell *in vivo* patch-clamp recordings were performed via a resistance-guided (blind) method

468 as previously described (Ishikawa et al., 2015; Rancz et al., 2007). Voltage clamp and current

469 clamp recordings were made from granule cells at a depth of 200–400 μm in crus II of the

470 cerebellar cortex by using a Multiclamp 700B amplifier (Molecular Devices). Data were low-pass

471 filtered at 6 kHz and acquired at 50 kHz using a USB-6259 interface (National Instruments) and

472 Igor Pro with NIDAQ Tools MX (WaveMetrics). The internal solution contained (in mM) K-

473 methanesulfonate 135, KCl 7, HEPES 10, Mg-ATP 2, Na_2ATP 2, Na_2GTP 0.5, and EGTA 0.05 or

474 0.1 (pH adjusted to 7.2 with KOH), giving an estimated chloride reversal potential of -69 mV. This

475 enabled excitatory synaptic currents to be observed in isolation by voltage clamping at -70 mV and

476 inhibitory synaptic currents to be observed at 0 mV. The liquid junction potential was not corrected.

477 In a subset of experiments, biocytin 0.5% was added to the internal solution. The granule cells

478 were identified by a small membrane capacitance (C_m) (less than 7 pF) and a lack of periodic

479 spontaneous firings. The mossy fiber boutons were identified by the occurrence of high-frequency

480 bursts and a lack of synaptic potentials (Rancz et al., 2007). Patch pipettes had resistances of 5–8

481 MΩ, and series resistances (R_s) were typically 30–50 MΩ. Cells with high R_s were excluded to

482 keep the access time constant ($R_s \cdot C_m$) at <0.3 ms. Extracellular unit recordings from Purkinje cells

483 were made with glass electrodes (5 MΩ) filled with saline. The Purkinje cells were identified by the

484 occurrence of SS and CS. Field potential recordings were conducted using a tungsten electrode (1

485 MΩ, TM31A10; WPI). Neocortical field potentials were recorded at a depth of 550–650 μm in the

486 primary somatosensory area for the upper lip (3.8 mm lateral and 0 mm rostrocaudal from bregma)

487 unless otherwise noted. Cerebellar field potentials were recorded in the GCL at a depth of 300–500

488 μm in the crus II area. In VGAT-ChR2 mice, the somatosensory cortex was optogenetically

17

489 inactivated by illuminating the surface with an optic fiber (0.39 NA, Ø400 μm, FT400EMT;

490 Thorlabs) coupled to a high-power blue LED (470 nm, M470D2; Thorlabs). The optic fiber was

491 bundled with a single tungsten electrode, and the tip of the electrode was 800 μm ahead of that of

492 the optic fiber so that the tip of the optic fiber was above the surface of the brain during the

493 recording. To record from visually identified bands in Aldoc-Venus mice, the angle of electrode was

494 carefully adjusted to be perpendicular to the brain surface, and the center of each band was

495 targeted. However, due to the limited spatial specificity inherent in field potential recording

496 (Kajikawa and Schroeder, 2011), contamination of field potentials from neighboring bands was not

497 fully excluded. For whole-cell recordings from those mice, only 5+, 5-, 6+, and 7+ bands, which

498 were relatively wide and easy to identify, were used. Tactile stimulation (air puff, 50 ms, 90 mmHg

499 at the source) was applied to the left upper lip with a solenoid valve (FAB31-8-3-12C-1; CKD,

500 Aichi, Japan) controlled via the USB-6259 interface as described above.

501

502 **Analysis**

503 To analyze field potential recordings, the peak amplitude from the baseline was measured. In

504 ketamine/xylazine anesthetized mice, the baseline for the cerebellar late component was set at the

505 beginning of the late component, which could be readily identified. In awake mice and mice

506 anesthetized with a mixture of medetomidine (0.3 mg/kg), midazolam (4 mg/kg), and butorphanol

507 (5 mg/kg) or with isoflurane, the late component was measured as the mean amplitude 18–23 ms

508 from the stimulation onset after subtracting the extrapolated decay component of the early

509 response (a single exponential curve common under control and photoinhibited conditions).

510 EPSCs and action potentials in whole-cell recordings were detected using TaroTools

511 (https://sites.google.com/site/tarotoolsregister/), a threshold-based algorithm in Igor Pro

512 (WaveMetrics). The event number (for both synaptic events and action potentials) evoked by

513 stimulation was counted (baseline subtracted) in a time window adjusted for each cell to include all

514 evoked events but to minimize contamination of spontaneous events. The beginning of the time

515 window was adjusted to between 0 and 5 ms from the onset of stimulation, and the end of the time

516 window was between 50 and 60 ms. The border between the early and the late phases was

517 adjusted to between 16 and 20 ms so that the border matched the valley of the time histogram.

518 The synaptic charge was measured as the integral of the averaged current trace (baseline

519 subtracted and sign reversed). The latency of the sensory response was defined as the time from

520 the stimulus onset to the first EPSC event. Data are presented as means ± SEMs. Statistical

521 significance was tested by using Wilcoxon signed-rank tests for paired samples and Wilcoxon–

522 Mann–Whitney tests for independent samples.

523

524 **Acknowledgments**

525   The authors are grateful to Toshihiko Momiyama, Soichi Nagao, and Hirofumi Tokuoka for their

526   generous support, to Tadaharu Tsumoto and Kazuhiro Sohya for their help in obtaining VGAT-

527   ChR2 mice, and to Miwa Takagi for technical assistance. This work was supported by JSPS

528   KAKENHI (grant number 18K06529), MEXT-Supported Program for the Strategic Research

529   Foundation at Private Universities (S1311009), and the Jikei University Research Fund.

530

531   **Author contributions**

532   Conceptualization, M.S. and T.I.; Methodology, M.S. and T.I.; Software, T.I.; Formal Analysis, T.I.;

533   Investigation, M.S. and T.I.; Resources, I.S.; Writing –Original Draft, T.I.; Writing –Review &

534   Editing, M.S. and I.S.; Supervision, I.S. and T.I.; Project Administration, T.I.; Funding Acquisition,

535   M.S., I.S. and T.I.

536

537   **Declaration of interests**

538   The authors declare no competing interests.

539   **REFERENCES**

Albus, J.S. (1971). A theory of cerebellar function. Mathematical Biosciences *10*, 25–61.

Allen, G.I., and Tsukahara, N. (1974). Cerebrocerebellar communication systems. Physiol. Rev. *54*, 957–1006.

Allen, G.I., Azzena, G.B., and Ohno, T. (1974). Somatotopically organized inputs from fore- and hindlimb areas of sensorimotor cortex to cerebellar Purkyně cells. Exp Brain Res *20*, 255–272.

Bengtsson, F., and Jörntell, H. (2007). Ketamine and xylazine depress sensory-evoked parallel fiber and climbing fiber responses. J. Neurophysiol. *98*, 1697–1705.

Bengtsson, F., and Jörntell, H. (2009). Sensory transmission in cerebellar granule cells relies on similarly coded mossy fiber inputs. Proc. Natl. Acad. Sci. U.S.A. *106*, 2389–2394.

Bennett-Clarke, C.A., Chiaia, N.L., Jacquin, M.F., and Rhoades, R.W. (1992). Parvalbumin and calbindin immunocytochemistry reveal functionally distinct cell groups and vibrissa-related patterns in the trigeminal brainstem complex of the adult rat. J. Comp. Neurol. *320*, 323–338.

Biswas, M.S., Luo, Y., Sarpong, G.A., and Sugihara, I. (2019). Divergent projections of single pontocerebellar axons to multiple cerebellar lobules in the mouse. J. Comp. Neurol.

Blot, A., de Solages, C., Ostojic, S., Szapiro, G., Hakim, V., and Léna, C. (2016). Time-invariant feed-forward inhibition of Purkinje cells in the cerebellar cortex in vivo. J. Physiol. (Lond.) *594*, 2729–2749.

Bostan, A.C., Dum, R.P., and Strick, P.L. (2013). Cerebellar networks with the cerebral cortex and basal ganglia. Trends in Cognitive Sciences *17*, 241–254.

Bower, J.M., and Woolston, D.C. (1983). Congruence of spatial organization of tactile projections to granule cell and Purkinje cell layers of cerebellar hemispheres of the albino rat: vertical organization of cerebellar cortex. J. Neurophysiol. *49*, 745–766.

Bower, J.M., Beermann, D.H., Gibson, J.M., Shambes, G.M., and Welker, W. (1981). Principles of organization of a cerebro-cerebellar circuit. Micromapping the projections from cerebral (SI) to cerebellar (granule cell layer) tactile areas of rats. Brain Behav. Evol. *18*, 1–18.

Brown, I.E., and Bower, J.M. (2002). The influence of somatosensory cortex on climbing fiber responses in the lateral hemispheres of the rat cerebellum after peripheral tactile stimulation. J. Neurosci. *22*, 6819–6829.

Carlton, S.M., Leichnetz, G.R., and Mayer, J.D. (1982). Projections from the nucleus parafascicularis prerubralis to medullary raphe nuclei and inferior olive in the rat: a horseradish peroxidase and autoradiography study. Neurosci. Lett. *30*, 191–197.

Cathala, L., Brickley, S., Cull-Candy, S., and Farrant, M. (2003). Maturation of EPSCs and intrinsic membrane properties enhances precision at a cerebellar synapse. J. Neurosci. *23*, 6074–6085.

Cayco-Gajic, N.A., and Silver, R.A. (2019). Re-evaluating Circuit Mechanisms Underlying Pattern Separation. Neuron *101*, 584–602.

Chabrol, F.P., Arenz, A., Wiechert, M.T., Margrie, T.W., and DiGregorio, D.A. (2015). Synaptic diversity enables temporal coding of coincident multisensory inputs in single neurons. Nat. Neurosci. *18*, 718–727.

Chadderton, P., Margrie, T.W., and Häusser, M. (2004). Integration of quanta in cerebellar granule cells during sensory processing. Nature *428*, 856–860.

D'Angelo, E., Solinas, S., Mapelli, J., Gandolfi, D., Mapelli, L., and Prestori, F. (2013). The cerebellar Golgi cell and spatiotemporal organization of granular layer activity. Front Neural Circuits *7*, 93.

Dean, P., Porrill, J., Ekerot, C.-F., and Jörntell, H. (2010). The cerebellar microcircuit as an adaptive filter: experimental and computational evidence. Nat. Rev. Neurosci. *11*, 30–43.

Diwakar, S., Magistretti, J., Goldfarb, M., Naldi, G., and D'Angelo, E. (2009). Axonal Na+ channels ensure fast spike activation and back-propagation in cerebellar granule cells. J. Neurophysiol. *101*, 519–532.

Duguid, I., Branco, T., London, M., Chadderton, P., and Häusser, M. (2012). Tonic inhibition enhances fidelity of sensory information transmission in the cerebellar cortex. J. Neurosci. *32*, 11132–11143.

Duguid, I., Branco, T., Chadderton, P., Arlt, C., Powell, K., and Häusser, M. (2015). Control of cerebellar granule cell output by sensory-evoked Golgi cell inhibition. Proc. Natl. Acad. Sci. U.S.A. *112*, 13099–13104.

Fujita, H., Aoki, H., Ajioka, I., Yamazaki, M., Abe, M., Oh-Nishi, A., Sakimura, K., and Sugihara, I. (2014). Detailed expression pattern of aldolase C (Aldoc) in the cerebellum, retina and other areas of the CNS studied in Aldoc-Venus knock-in mice. PLoS ONE *9*, e86679.

Giovannucci, A., Badura, A., Deverett, B., Najafi, F., Pereira, T.D., Gao, Z., Ozden, I., Kloth, A.D., Pnevmatikakis, E., Paninski, L., et al. (2017). Cerebellar granule cells acquire a widespread predictive feedback signal during motor learning. Nat. Neurosci. *20*, 727–734.

Guo, Z.V., Li, N., Huber, D., Ophir, E., Gutnisky, D., Ting, J.T., Feng, G., and Svoboda, K. (2014). Flow of cortical activity underlying a tactile decision in mice. Neuron *81*, 179–194.

Hamann, M., Rossi, D.J., and Attwell, D. (2002). Tonic and spillover inhibition of granule cells control information flow through cerebellar cortex. Neuron *33*, 625–633.

Harris, K.D., and Thiele, A. (2011). Cortical state and attention. Nat. Rev. Neurosci. *12*, 509–523.

Hines, M.L., and Carnevale, N.T. (1997). The NEURON simulation environment. Neural Comput *9*, 1179–1209.

Huang, C.-C., Sugino, K., Shima, Y., Guo, C., Bai, S., Mensh, B.D., Nelson, S.B., and Hantman, A.W. (2013). Convergence of pontine and proprioceptive streams onto multimodal cerebellar granule cells. Elife *2*, e00400.

Ishikawa, T., Shimuta, M., and Häusser, M. (2015). Multimodal sensory integration in single cerebellar granule cells in vivo. Elife *4*.

Jelitai, M., Puggioni, P., Ishikawa, T., Rinaldi, A., and Duguid, I. (2016). Dendritic excitation-inhibition balance shapes cerebellar output during motor behaviour. Nat Commun *7*, 13722.

Kajikawa, Y., and Schroeder, C.E. (2011). How local is the local field potential? Neuron *72*, 847–858.

Kratochwil, C.F., Maheshwari, U., and Rijli, F.M. (2017). The Long Journey of Pontine Nuclei Neurons: From Rhombic Lip to Cortico-Ponto-Cerebellar Circuitry. Front Neural Circuits *11*, 33.

Kubo, R., Aiba, A., and Hashimoto, K. (2018). The anatomical pathway from the mesodiencephalic junction to the inferior olive relays perioral sensory signals to the cerebellum in the mouse. J. Physiol. (Lond.) *596*, 3775–3791.

Leergaard, T.B., and Bjaalie, J.G. (2007). Topography of the complete corticopontine projection: from experiments to principal Maps. Front Neurosci *1*, 211–223.

Leergaard, T.B., Lillehaug, S., De Schutter, E., Bower, J.M., and Bjaalie, J.G. (2006). Topographical organization of pathways from somatosensory cortex through the pontine nuclei to tactile regions of the rat cerebellar hemispheres. Eur. J. Neurosci. *24*, 2801–2812.

Li, N., Chen, T.-W., Guo, Z.V., Gerfen, C.R., and Svoboda, K. (2015). A motor cortex circuit for motor planning and movement. Nature *519*, 51–56.

Li, N., Daie, K., Svoboda, K., and Druckmann, S. (2016). Robust neuronal dynamics in premotor cortex during motor planning. Nature *532*, 459–464.

Mapelli, L., Solinas, S., and D'Angelo, E. (2014). Integration and regulation of glomerular inhibition in the cerebellar granular layer circuit. Front Cell Neurosci *8*, 55.

Marr, D. (1969). A theory of cerebellar cortex. J. Physiol. (Lond.) *202*, 437–470.

Matyas, F., Sreenivasan, V., Marbach, F., Wacongne, C., Barsy, B., Mateo, C., Aronoff, R., and Petersen, C.C.H. (2010). Motor control by sensory cortex. Science *330*, 1240–1243.

Millar, J.A., Barratt, L., Southan, A.P., Page, K.M., Fyffe, R.E., Robertson, B., and Mathie, A. (2000). A functional role for the two-pore domain potassium channel TASK-1 in cerebellar granule neurons. Proc. Natl. Acad. Sci. U.S.A. *97*, 3614–3618.

Miyamoto, D., Hirai, D., Fung, C.C.A., Inutsuka, A., Odagawa, M., Suzuki, T., Boehringer, R., Adaikkan, C., Matsubara, C., Matsuki, N., et al. (2016). Top-down cortical input during NREM sleep consolidates perceptual memory. Science *352*, 1315–1318.

Mohajerani, M.H., Chan, A.W., Mohsenvand, M., LeDue, J., Liu, R., McVea, D.A., Boyd, J.D., Wang, Y.T., Reimers, M., and Murphy, T.H. (2013). Spontaneous cortical activity alternates between motifs defined by regional axonal projections. Nat. Neurosci. *16*, 1426–1435.

Morissette, J., and Bower, J.M. (1996). Contribution of somatosensory cortex to responses in the rat cerebellar granule cell layer following peripheral tactile stimulation. Exp Brain Res *109*, 240–250.

Na, J., Sugihara, I., and Shinoda, Y. (2019). The entire trajectories of single pontocerebellar axons and their lobular and longitudinal terminal distribution patterns in multiple aldolase C positive compartments of the rat cerebellar cortex. J. Comp. Neurol.

Naus, C., Flumerfelt, B.A., and Hrycyshyn, A.W. (1985). An anterograde HRP-WGA study of aberrant corticorubral projections following neonatal lesions of the rat sensorimotor cortex. Exp Brain Res *59*, 365–371.

Pachitariu, M., Lyamzin, D.R., Sahani, M., and Lesica, N.A. (2015). State-dependent population coding in primary auditory cortex. J. Neurosci. *35*, 2058–2073.

Poulet, J.F.A., and Crochet, S. (2018). The Cortical States of Wakefulness. Front Syst Neurosci *12*, 64.

Powell, K., Mathy, A., Duguid, I., and Häusser, M. (2015). Synaptic representation of locomotion in single cerebellar granule cells. Elife *4*.

Proville, R.D., Spolidoro, M., Guyon, N., Dugué, G.P., Selimi, F., Isope, P., Popa, D., and Léna, C. (2014). Cerebellum involvement in cortical sensorimotor circuits for the control of voluntary movements. Nat. Neurosci. *17*, 1233–1239.

Provini, L., Redman, S., and Strata, P. (1968). Mossy and climbing fibre organization on the anterior lobe of the cerebellum activated by forelimb and hindlimb areas of the sensorimotor cortex. Exp Brain Res *6*, 216–233.

Ramanathan, D.S., Gulati, T., and Ganguly, K. (2015). Sleep-Dependent Reactivation of Ensembles in Motor Cortex Promotes Skill Consolidation. PLoS Biol. *13*, e1002263.

Rancz, E.A., Ishikawa, T., Duguid, I., Chadderton, P., Mahon, S., and Häusser, M. (2007). High-fidelity transmission of sensory information by single cerebellar mossy fibre boutons. Nature *450*, 1245–1248.

Ros, H., Sachdev, R.N.S., Yu, Y., Sestan, N., and McCormick, D.A. (2009). Neocortical networks entrain neuronal circuits in cerebellar cortex. J. Neurosci. *29*, 10309–10320.

Sasaki, K., Oka, H., Kawaguchi, S., Jinnai, K., and Yasuda, T. (1977). Mossy fibre and climbing fibre responses produced in the cerebeller cortex by stimulation of the cerebral cortex in monkeys. Exp Brain Res *29*, 419–428.

Schmahmann, J.D., Guell, X., Stoodley, C.J., and Halko, M.A. (2019). The Theory and Neuroscience of Cerebellar Cognition. Annu. Rev. Neurosci. *42*, 337–364.

Sillitoe, R.V., Fu, Y., and Watson, C. (2012). Chapter 11 - Cerebellum. In The Mouse Nervous System, (San Diego: Academic Press), pp. 360–397.

Solowska, J.M., Mazurek, A., Weinberger, L., and Baird, D.H. (2002). Pontocerebellar axon guidance: neuropilin-1- and semaphorin 3A-sensitivity gradients across basilar pontine nuclei and semaphorin 3A variation across cerebellum. Mol. Cell. Neurosci. *21*, 266–284.

Steindler, D.A. (1985). Trigeminocerebellar, trigeminotectal, and trigeminothalamic projections: a double retrograde axonal tracing study in the mouse. J. Comp. Neurol. *237*, 155–175.

Sugihara, I., and Shinoda, Y. (2004). Molecular, topographic, and functional organization of the cerebellar cortex: a study with combined aldolase C and olivocerebellar labeling. J. Neurosci. *24*, 8771–8785.

Tabuchi, S., Gilmer, J.I., Purba, K., and Person, A.L. (2018). Pathway specific drive of cerebellar Golgi cells reveals integrative rules of cortical inhibition. J. Neurosci.

Tahon, K., Wijnants, M., De Schutter, E., and Maex, R. (2011). Current source density correlates of cerebellar Golgi and Purkinje cell responses to tactile input. J. Neurophysiol. *105*, 1327–1341.

Tamamaki, N., and Tomioka, R. (2010). Long-Range GABAergic Connections Distributed throughout the Neocortex and their Possible Function. Front Neurosci *4*, 202.

Valera, A.M., Binda, F., Pawlowski, S.A., Dupont, J.-L., Casella, J.-F., Rothstein, J.D., Poulain, B., and Isope, P. (2016). Stereotyped spatial patterns of functional synaptic connectivity in the cerebellar cortex. Elife *5*.

Vos, B.P., Volny-Luraghi, A., and De Schutter, E. (1999). Cerebellar Golgi cells in the rat: receptive fields and timing of responses to facial stimulation. Eur. J. Neurosci. *11*, 2621–2634.

Wagner, M.J., Kim, T.H., Savall, J., Schnitzer, M.J., and Luo, L. (2017). Cerebellar granule cells encode the expectation of reward. Nature *544*, 96–100.

Wagner, M.J., Kim, T.H., Kadmon, J., Nguyen, N.D., Ganguli, S., Schnitzer, M.J., and Luo, L. (2019). Shared Cortex-Cerebellum Dynamics in the Execution and Learning of a Motor Task. Cell *177*, 669-682.e24.

Watson, T.C., and Apps, R. (2019). Cerebro-Cerebellar Connections. In Handbook of the Cerebellum and Cerebellar Disorders, M. Manto, D. Gruol, J. Schmahmann, N. Koibuchi, and R. Sillitoe, eds. (Cham: Springer International Publishing), pp. 1–26.

Welker, W. (1987). Spatial organization of somatosensory projections to granule cell cerebellar cortex: functional and connectional implications of fractured somatotopy (summary of Wisconsin studies). New Concepts in Cerebellar Neurobiology 239–280.

Woolston, D.C., Kassel, J., and Gibson, J.M. (1981). Trigeminocerebellar mossy fiber branching to granule cell layer patches in the rat cerebellum. Brain Res. *209*, 255–269.

Zhang, F.-X., Ge, S.-N., Dong, Y.-L., Shi, J., Feng, Y.-P., Li, Y., Li, Y.-Q., and Li, J.-L. (2018). Vesicular glutamate transporter isoforms: The essential players in the somatosensory systems. Prog. Neurobiol. *171*, 72–89.

Zhao, S., Ting, J.T., Atallah, H.E., Qiu, L., Tan, J., Gloss, B., Augustine, G.J., Deisseroth, K., Luo, M., Graybiel, A.M., et al. (2011). Cell type–specific channelrhodopsin-2 transgenic mice for optogenetic dissection of neural circuitry function. Nat. Methods *8*, 745–752.
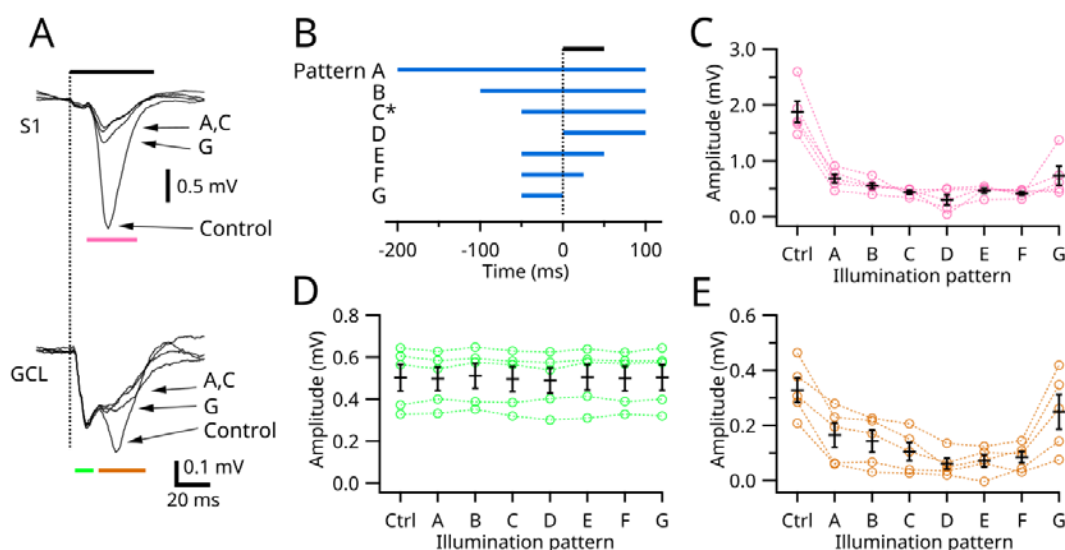
540 **Supplemental Figures**

541

542 **Figure S1. Exploration of temporal patterns of S1 photoinhibition.**
543 (A) Representative recordings of field potential in S1 (top) and cerebellar GCL (bottom). The averages
544 from 20 traces in each stimulation pattern are shown.
545 (B) Temporal patterns of the light illumination. The patterns B, D, E, and F are omitted in (A) for clarity.
546 Black bar indicates the duration of air puff, whose onset is indicated by the vertical dotted line.
547 (C–E) The peak amplitudes of S1 field potentials (C) and the early (D) and the late (E) components of
548 cerebellar GCL field potentials ($n = 5$). Means ± SEMs are presented as black bars and lines,
549 respectively.

23
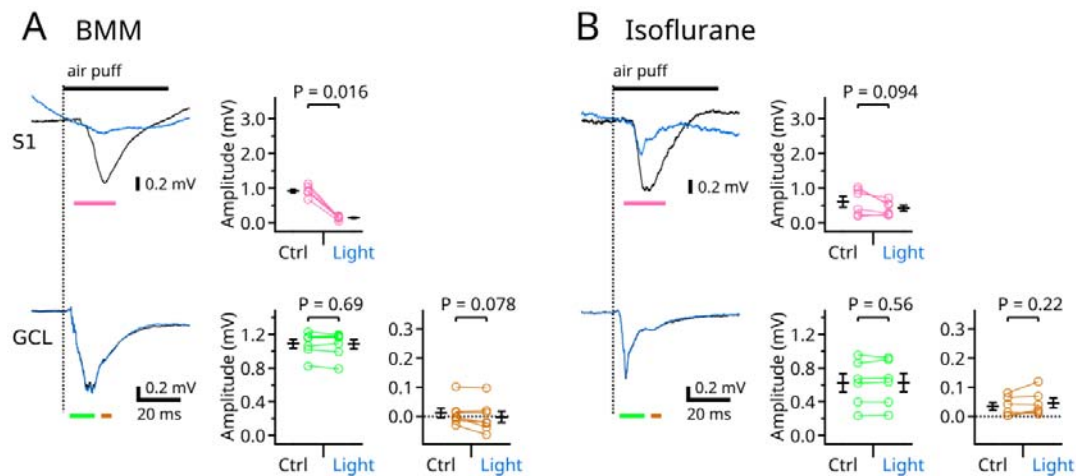
550 **Figure S2. Effects of anesthetics on the cerebral and cerebellar responses.**
551 (A) The same experiments as described for Figures 1E and 1F, but the mice were anesthetized with a
552 mixture of medetomidine (0.3 mg/kg), midazolam (4 mg/kg), and butorphanol (5 mg/kg) (BMM).
553 (B) The same as in (A), but the mice are anesthetized with isoflurane (2%).
554 Means ± SEMs are presented as black bars and lines, respectively.
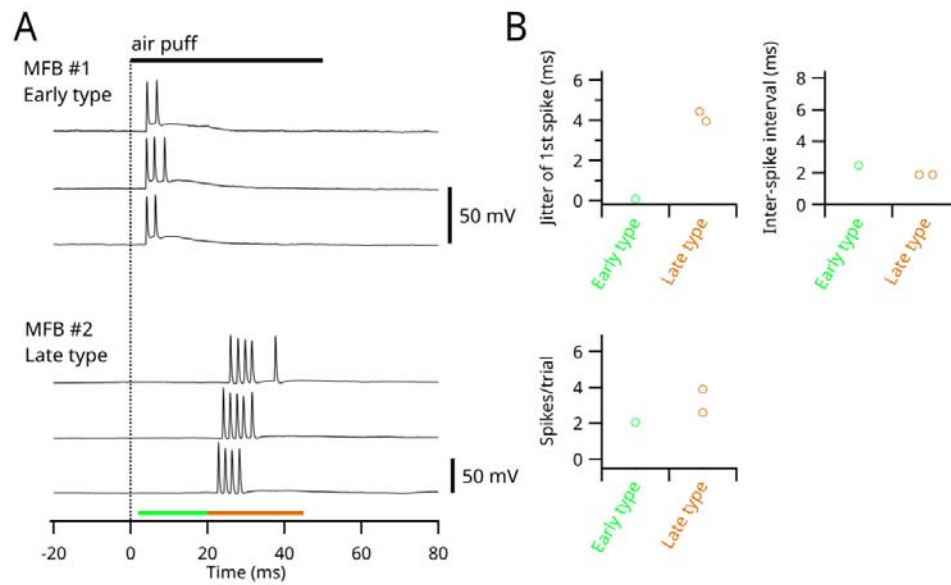
Figure S3. Sensory responses in putative mossy fiber boutons.

(A) Whole-cell current clamp recordings from putative mossy fiber boutons (MFB; n = 3). MFB #1 was from a VGAT-ChR2 mouse, whereas MFB #2 was from an Aldoc-Venus mouse. Firing of MFB #1 was not affected by photoinhibition of S1 (not displayed). Three sample traces from each MFB are shown. MFBs were categorized as the early or the late type on the basis of their timing of firing.

(B) Spike patterns were analyzed in the same manner as described for Figures 2D, 2E, and 2F.

561
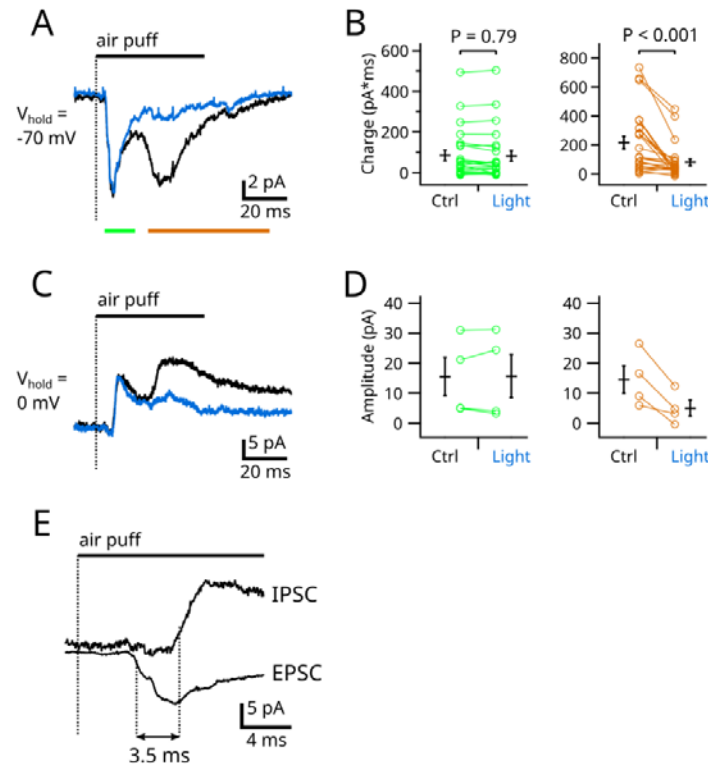
Figure S4. Extra data from whole-cell voltage clamp experiments.

(A) Average traces of EPSCs in all 24 granule cells presented in Figure 2.

(B) Synaptic charges (integral of the synaptic current, $n = 24$) measured for the time periods indicated in (A). The synaptic charges during the late phase (right, brown) may contain the tails of the early components (left, green).

(C) Average traces of IPSCs from four granule cells voltage clamped at 0 mV (the reversal potential for the glutamatergic current).

(D) The amplitudes of IPSCs ($n = 4$).

(E) Comparison of onsets of an EPSC and IPSC. Control traces in (A) and (C) are shown together. The onset (20% rising point) of the averaged traces had a 3.5 ms difference.

Means ± SEMs are presented as black bars and lines, respectively.

26
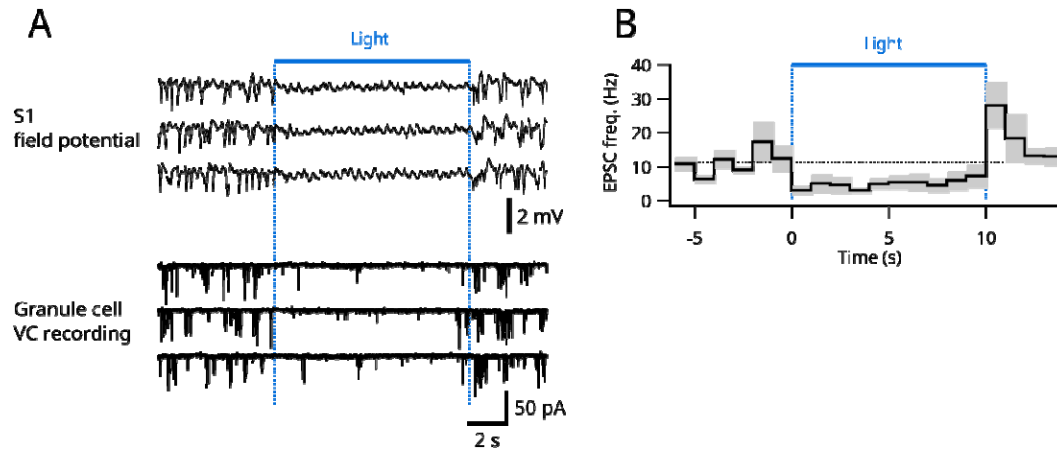
Figure S5. Effect of S1 photoinhibition on spontaneous EPSC in granule cells.

(A) Representative recordings; simultaneous field potential recordings from S1 (top) and whole-cell voltage clamp recording from a granule cell (bottom). Long (10 s) blue light applications were repeated five times, but three trials are displayed.

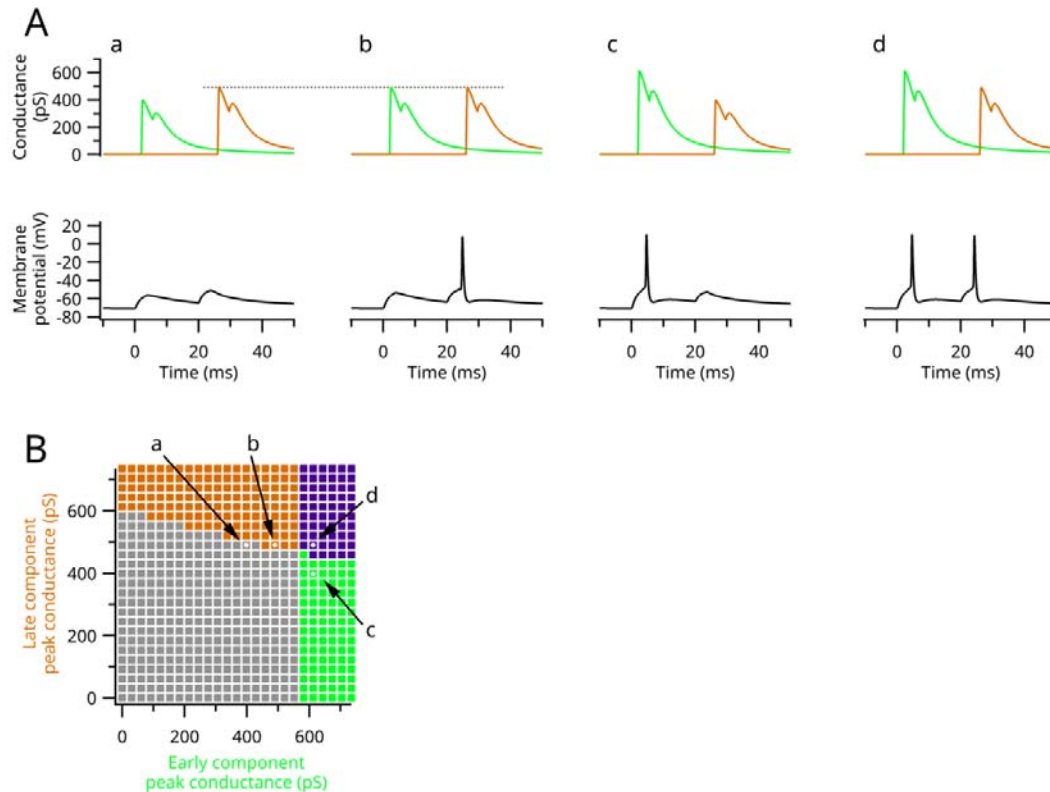(B) Frequencies of spontaneous EPSCs (average from three granule cells) are displayed. Shading indicates SEMs.

Figure S6. Computer simulation of action potential generation in granule cells.

(A) Four representative patterns of simulation. Top, AMPA-type synaptic conductance. Bottom, resulting membrane potential at the soma. A realistic model of a granule cell was used as published by (Diwakar et al., 2009) for the NEURON simulation environment (Hines and Carnevale, 1997) without modifications except for AMPA and NMDA conductances, which were systematically changed while the NMDA:AMPA ratio was kept constant (0.2) (Cathala et al., 2003; Powell et al., 2015). Excitatory synaptic conductances, each of which consists of two synaptic events with a 3 ms interval, were applied to two dendrites with a separation of 20 ms. Inhibitory synaptic conductances, each of which consists of a single synaptic event with a 3.5 ms delay from the onset of excitatory synaptic conductance, were applied with a separation of 20 ms and a constant maximal conductance (756.35 pS).

(B) The overall profile of spiking patterns triggered by various synaptic conductances. A plot resembling that in Figure 2B, but where the colors indicate the resulting spike patterns. White dots indicate the cases presented in (A).
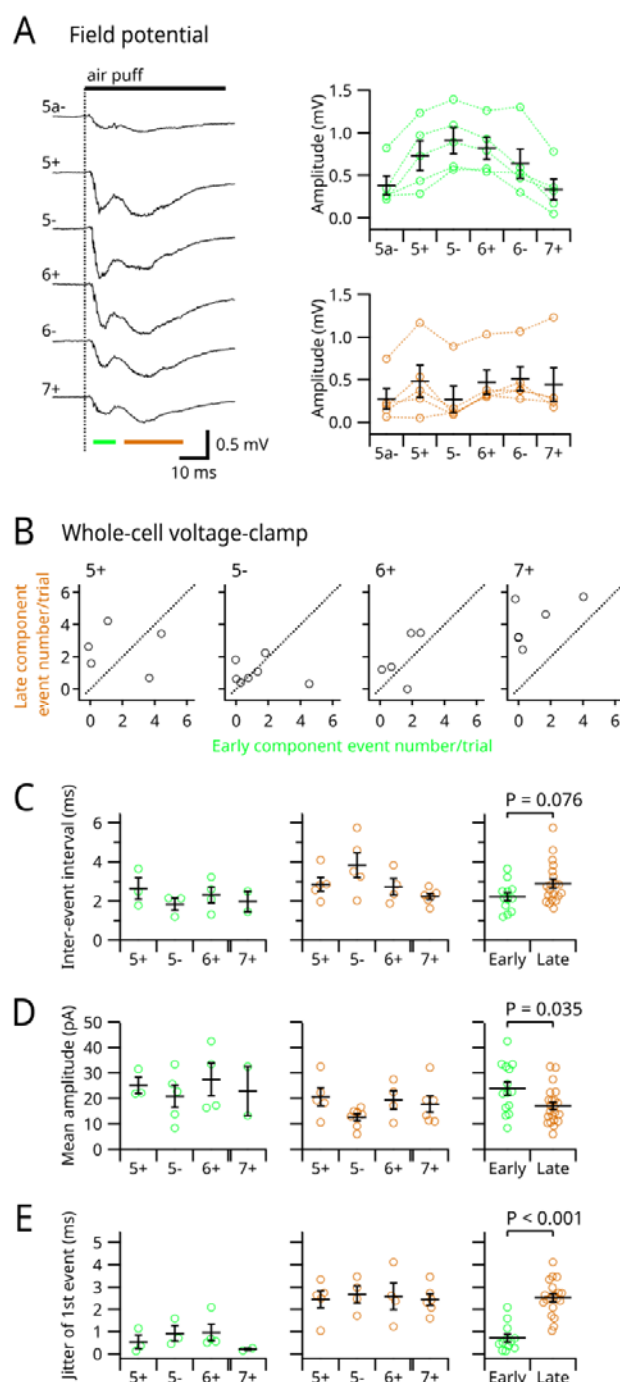
Figure S7. Extra data from experiments using Aldoc-Venus mice.

(A) Left, representative field potential recordings from six different bands in crus II. Right, pooled data from five mice. The amplitudes of early (top) and late responses were measured during the times indicated by the colored bars in the left panel.

(B) The numbers of evoked EPSC events in the early and the late phases were compared in individual bands. The same data as in Figure 4C were used. Dotted lines indicate unity.

(C–E) The median interevent intervals (C), the mean amplitudes (D), and the jitter (the standard deviation of the timing) (E) of EPSCs in various bands in the early (left) and the late (right) phases. The right panels show pooled data from all bands.

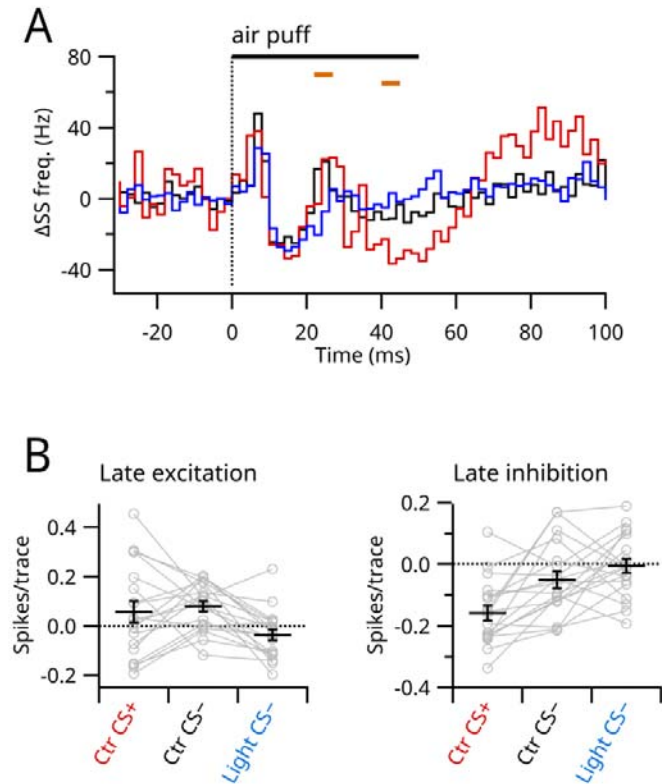Means ± SEMs are presented as black bars and lines, respectively.

Figure S8. Detailed analysis of the interaction of SS and CS in Purkinje cells.

(A) Average time histogram (2 ms bin, $n = 19$) of SS from trials with CS responses (red) and without CS responses (black) under the control condition and those without CS responses during photoinhibition of S1 (blue) are shown. In S1 photoinhibition, trials with CS responses were rare and therefore omitted in this analysis.

(B) SS numbers were measured during the times indicated by bars in (A), the same timings as in Figure 5C. Means ± SEMs are presented as black bars and lines, respectively.
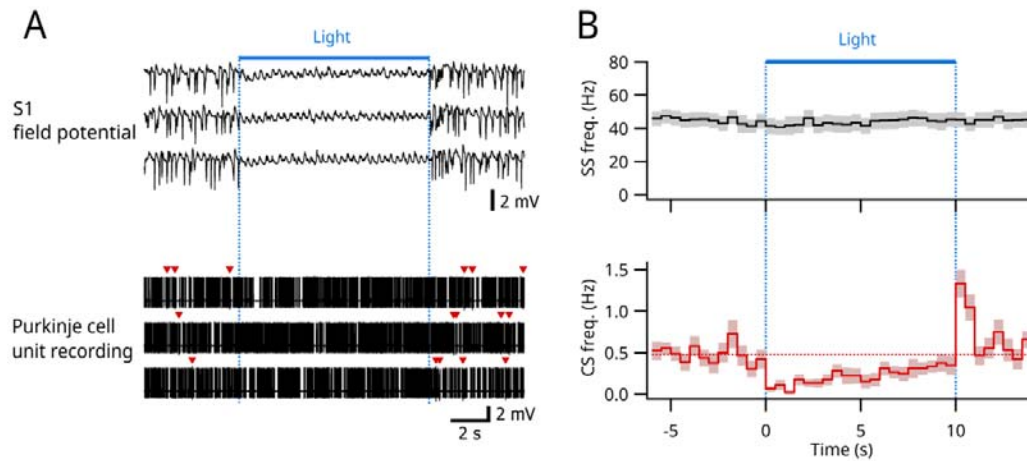
609 **Figure S9. Effects of S1 photoinhibition on spontaneous SS and CS in Purkinje cells.**
610 (A) Representative recordings; simultaneous field potential recordings from S1 (top) and unit recordings
611 from a Purkinje cell (bottom). Long (10 s) blue light applications were repeated six times, but three trials
612 are displayed. Red arrowheads indicate CS.
613 (B) Averages from 18 Purkinje cells. Spontaneous frequencies of SS (top) and CS (bottom) are
614 displayed. Shading indicates SEMs.

31